Naval Research Laboratory

Washington, DC 20375-5320

U.S. NAVAL RESEARCH LABORATORY

Novel Microwave Remote Sensing Techniques Using Small Satellite Constellations

TANISH HIMANI

Passive Microwave Branch
Remote Sensing Division

February 8, 2022

REPORT DOCUMENTATION PAGE

1. REPORT DATE *(DD-MM-YYYY)*	2. REPORT TYPE	3. DATES COVERED *(From - To)*
08-02-2022	NRL Memorandum Report	01-04-2019 – 01-04-2021

4. TITLE AND SUBTITLE

Novel Microwave Remote Sensing Techniques Using Small Satellite Constellations

5a. CONTRACT NUMBER

5b. GRANT NUMBER

5c. PROGRAM ELEMENT NUMBER
NISE

6. AUTHOR(S)

Tanish Himani

5d. PROJECT NUMBER

5e. TASK NUMBER

5f. WORK UNIT NUMBER
N2T5

7. PERFORMING ORGANIZATION NAME(S) AND ADDRESS(ES)

Naval Research Laboratory
4555 Overlook Avenue, SW
Washington, DC 20375-5320

8. PERFORMING ORGANIZATION REPORT NUMBER

NRL/7220/MR--2022/1

9. SPONSORING / MONITORING AGENCY NAME(S) AND ADDRESS(ES)

Naval Research Laboratory
4555 Overlook Avenue, SW
Washington, DC 20375-5320

10. SPONSOR / MONITOR'S ACRONYM(S)

NRL-NISE

11. SPONSOR / MONITOR'S REPORT NUMBER(S)

12. DISTRIBUTION / AVAILABILITY STATEMENT

DISTRIBUTION STATEMENT A: Approved for public release; distribution is unlimited.

13. SUPPLEMENTARY NOTES
Karles Fellowship

14. ABSTRACT

In this report, the well-established Backus–Gilbert resolution enhancement algorithm for passive microwave sensors is applied to a novel distributed spacecraft geometry. While this geometry allows for significantly higher sampling densities and redundancy, the small spacecraft platform comes with more pronounced errors. The results show that resolution enhancement is possible using a distributed geometry even in the presence of worst case errors typical of current small spacecraft components. Experience from this work is then applied to an upcoming 6.1 New Start which focuses on fusion of small satellite data, specifically GNSS reflectometry from NASA's Cyclone Global Navigation Satellite System (CYGNSS) constellation. The bulk of efforts were focused on creating a processing pipeline to download CYGNSS data via NASA's PO.DAAC system and process CYGNSS Bistatic Normalized Radar Cross Section (BNRCS) using a incidence angle correction for land/ vegetation measurements.

15. SUBJECT TERMS

Microwave radiometry	Small satellite	Resolution enhancement
CYGNSS	GNSS reflectometry	

16. SECURITY CLASSIFICATION OF:			17. LIMITATION OF ABSTRACT	18. NUMBER OF PAGES	19a. NAME OF RESPONSIBLE PERSON
a. REPORT	**b. ABSTRACT**	**c. THIS PAGE**	U	17	Tanish Himani
U	U	U			**19b. TELEPHONE NUMBER** *(include area code)*
					(202) 767-8253

This page intentionally left blank.

CONTENTS

This page intentionally left blank.

EXECUTIVE SUMMARY

This report presents research conducted by Tanish Himani under the Karles Fellowship for the period of April 1, 2019 through April 1, 2021. The majority of this work focuses on developing a microwave brightness temperature resolution enhancement algorithm for a distributed small satellite constellation (see *Publications* for published work referenced in this report). In the final year of the fellowship, the fellow focused some of his efforts towards preliminary studies for a newly funded 6.1 New Start for which he is a CO-I: "Fusion of Reflectometry and Radiometry for Satellite Remote Sensing of Surface Soil Moisture."

In this report, the well-established Backus–Gilbert resolution enhancement algorithm for passive microwave sensors is applied to a novel distributed spacecraft geometry. While this geometry allows for significantly higher sampling densities and redundancy, the small spacecraft platform comes with more pronounced errors in the knowledge of navigation, attitude, antenna pattern function, instrument noise, and instrument bias compared to a flagship mission. Imperfect knowledge of these errors is simulated to determine the feasibility of using a distributed small satellite constellation for resolution enhancement rather than a dedicated single spacecraft scanning system. The results show that resolution enhancement is possible using a distributed geometry even in the presence of worst case errors typical of current small spacecraft components. Also, depending on the distribution of errors between spacecraft, degradation of performance can be mitigated. Furthermore, increased sampling densities achieved in this configuration can provide insight into sub-footprint scale features. If temporally dynamic brightness temperatures are used, large spacecraft separation distances and high rates of brightness temperature variation are both shown to degrade reconstruction performance.

The 6.1 New Start also focuses on fusion of small satellite data, specifically GNSS reflectometry from NASA's Cyclone Global Navigation Satellite System (CYGNSS) constellation. For preliminary work for the 6.1 New Start, the bulk of efforts were focused on creating a processing pipeline to download CYGNSS data via NASA's PO.DAAC system and process CYGNSS Bistatic Normalized Radar Cross Section (BNRCS) using a incidence angle correction for land measurements. Furthermore, existing field data sets were brought into the pipeline to serve as a point of comparison. Establishing and validating this pipeline will prove useful for ensuring the 6.1 New Start has an established capability for accessing and processing CYGNSS data.

This page intentionally left blank.

NOVEL MICROWAVE REMOTE SENSING TECHNIQUES USING SMALL SATELLITE CONSTELLATIONS

1. INTRODUCTION

1.1 Small Satellites: Benefits

Small satellites are have evolved from being primarily an academic learning platform [1] to now a vital capability for much of the DoD, including the Navy. Multiple public and private companies now exist [2] which offer a full array of spacecraft services for hosted scientific payloads. Some of the obvious engineering benefits to a small spacecraft platform include lower cost, quicker development schedules, and the ability to purchase commercial off-the-shelf (COTS) components. One of the primary observational benefits to this platform is the ability to launch multiple spacecraft in order to achieve faster revisit times at a total lower mission cost. This distributed geometry is critical when observing phenomena that are fast-evolving or occur on a global scale [3]—[7]. Furthermore, small satellites can help fill observational sampling density gaps for flagship missions [8].

1.2 Small Satellites: Overcoming Limitations

Despite significant benefits, the limited available mass, volume, and power often constrain the spatial and radiometric resolution of hosted payloads [9]. These small spacecraft engineering constraints often take the form of knowledge of navigation states, attitude states, antenna characterization, and so on. For small satellites, this is especially true as the mass, volume, and power accommodations limit the quality of sensors and actuators onboard the spacecraft bus [20]. Furthermore, the limitations of the spacecraft bus can result in infrequent updates to the attitude and navigation solutions resulting in increased error between measurement updates.

The proposed methods to overcome these limitations include combining data from multiple small satellites within a constellation or combining data from small satellites and larger flagship missions in a more synergistic manner [10, 11], a process known as data fusion [12]. In the realm of passive microwave radiometry, these methods make use of partially correlated measurements from a single scanning (linear or conical) radiometer to solve the inverse ill-posed problem of super-resolution [13]–[18]. However, these methods often do not address the possibility of obtaining measurements from multiple spacecraft (rather than a single scanning sensor) or make assumptions that do not reflect engineering constraints of the observing system [19]. These engineering constraints can translate into image registration errors and could potentially degrade the ability to perform data fusion. While a single scanning system can use multiple observation passes to improve sampling density, this sacrifices the temporal resolution of the observed phenomenology [21]. This tradeoff can be mitigated if small spacecraft constellations are used instead of single sensor multi-pass observations [9].

The purpose of this work is to determine the feasibility and effectiveness of data fusion on microwave radiometric measurements using multiple small spacecraft in the presence of errors that may not otherwise exist in a flagship-class single scanning spacecraft. The analysis performed can help constrain system-level requirements necessary to successfully combine data sets for future mission architectures.

---

2. APPROACH

2.1   Backus-Gilbert Method

The Backus-Gilbert (BG) method is a well-established algorithm for performing microwave resolution enhancement for scanning (linear or conical) radiometers and scatterometers. Specifically, BG is a type of reconstruction algorithm that relies on partially correlated sampled observations to better reconstruct the original signal [21].

In this work, the geometry of simulated measurements is based on a hypothetical distributed 1-D satellite constellation rather than a linear- or conical-scanning system. The BG algorithm implemented in this work is based on [22] and is presented here in brief to highlight differences between the scanning and distributed architectures. BG reconstruction relies on finding an estimate of the brightness temperature at a given ground location by taking a weighted sum of "n" nearby antenna temperature measurements:

$$T_{B_{est}}(x_0) = \sum_{n=-I}^{I} a_n T_{A_n}$$

where T_{Best} is the brightness temperature estimate at some ground location x_0, T_A are nearby antenna temperature measurements, and **a** is a vector containing coefficients a_n that weight each antenna temperature measurement.

T_A is obtained by convolving the antenna gain pattern $G(x)$, also known as the antenna pattern function (APF), with the physical scene brightness temperature, T_B, over all ground locations, x, within the sensor field-of-view (FoV):

$$T_A = \int G(x)T_B(x)dx + T_{\text{noise}}.$$

In a scanning sensor, each T_A is a single measurement along a scan line. In a distributed geometry, T_A represents a single measurement from an individual spacecraft. Common implementations of BG insert noise into the **a** coefficients; however, this work takes a more physics based approach and inserts the noise, T_{noise}, directly into the antenna temperature measurements. Weighting coefficients, **a**, are:

$$\mathbf{a} = \frac{\mathbf{S}^{-1}\mathbf{u}}{\mathbf{u}^{\mathrm{T}}\mathbf{S}^{-1}\mathbf{u}}$$

where **S** is a positive definite matrix of convolved overlapping antenna gain functions and **u** is a vector whose components are individual satellite antenna gain patterns integrated over ground locations x within their respective FoV. The terms of **S** and **u** respectively are given by:

$$S_{ij} = \int_{\text{overlap}} G_i(x)G_j(x)J(x, x_0)dx.$$

$$u_i = \int G_i(x)dx.$$

In scanning sensors, each entry S_{ij} is integrated over the overlap bounds of the ith and j^{th} measurement in a single scan line, whereas, in the distributed geometry, S_{ij} is integrated over the overlap bounds of simultaneous measurements of the ith and j^{th} spacecrafts. Thus, $G_i(x)$ and $G_j(x)$ are the antenna gain patterns of the ith and j^{th} spacecrafts, respectively. $J(x, x_0)$ is a penalty function set to unity so that no region within the integration bounds is emphasized over any another [23].

2.2   Simulation Setup

2.2.1 Spacecraft Geometry

The first part of the experiment Although this work uses a 1-D configuration, all available parameters used are typical of small spacecraft orbital dynamics. Fig. 1 shows an example of the distributed small spacecraft architecture in the sensing configuration.
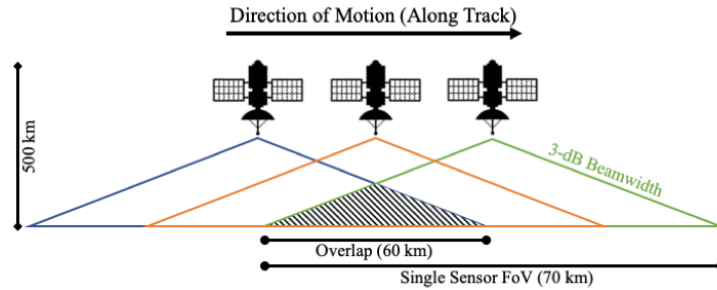

Fig. 1 — Example 1-D distributed spacecraft geometry (not to scale).

This geometry shows three small spacecraft, each with 70 km wide 3-dB footprints at an altitude of 500 km. The spacecraft is separated in-orbit by a constant 2.5 km and is designed with a baseline APF (seen in Section 2.2.2) such that the overlap bounds between all three APFs are 60 km. All the motions and reconstructions are done in the orbit along-track direction. It should be noted that all spacecrafts are assumed to be nadir pointing in their sensing configuration; meaning that no adjustment to the APF is necessary for configurations without attitude error.

While Fig. 1 shows an instantaneous measurement geometry, the full scene over which sampling occurs for reconstruction is 1400 km. All measurements assume that the Earth is locally flat for the overlap distance, and path length variations do not significantly affect the measured brightness temperature.

2.2.2 Antenna Pattern Function

Two APFs are considered in this work. The first is the baseline APF that consists of a truncated cosine function over a range   of −35 km ≤ x ≤ 35 km from nadir such that the bounds of the range represent the 3-dB dropoff point of a standard cosine function. This is an idealized APF that would be difficult to create with a real antenna. Fig. 2 shows the baseline APF that is used for all simulations except in the case of APF errors.
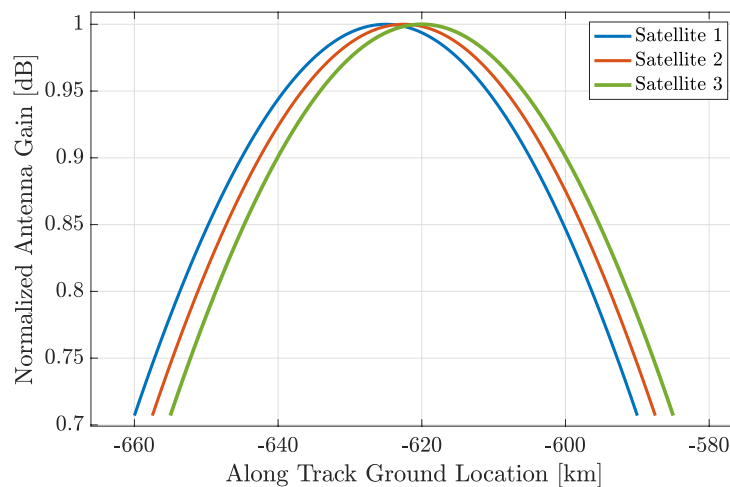

Fig. 2 — Example of baseline Earth projected APF (three spacecraft).

Fig. 3 shows the APFs used in the scenario where one APF is assumed in the algorithm but the true APF of the antenna has significant errors. This "true" APF is more realistic than the "assumed" APF although typical sidelobes in real antenna patterns are not as severe. While the APFs used in this work are fixed, note that computational requirements to compute BG coefficients for a distributed architecture with variable APFs could be significant.
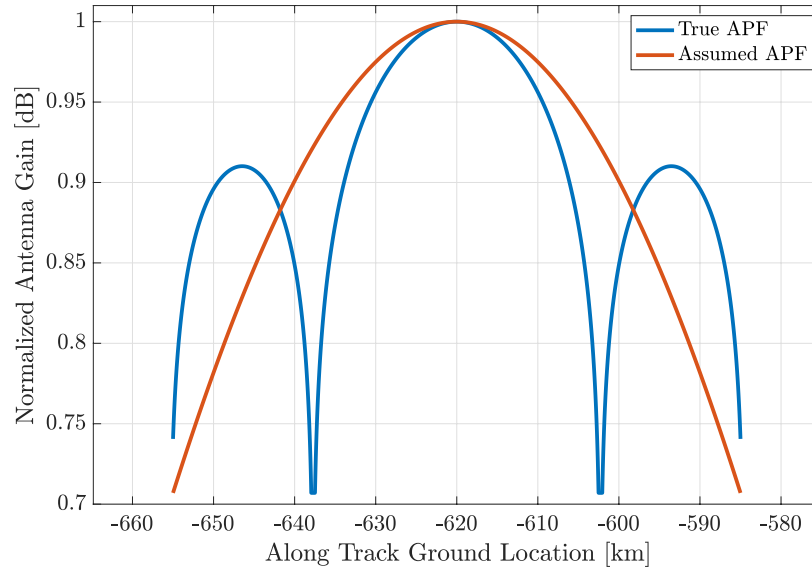

Fig. 3 — Example of true and assumed Earth projected APF (single spacecraft).

2.2.3 Performance Metrics

The analysis in the next section varies a single parameter of interest (e.g., APF error) while holding all other parameters constant in order to show the effects of a single parameter variation on the overall reconstructed profile. Since small satellites are affected by multiple simultaneous errors during flight, understanding the effect of individual errors can help direct engineering efforts during the mission design process.

These effects are quantified through the use of established statistical error metrics (standard deviation and r^2) and also goodness-of-fit metrics, such as total relative absolute (TRA) error [14] and the Nash–Sutcliffe model efficiency (NSE) coefficient [25]. In this work, we refer to both statistical and goodness-of-fit parameters as performance metrics.

3.   MODELING

Various types of errors were simulated in this work; sampling distance, noise, navigation, attitude, APF, etc. However, for brevity, only two scenarios are detailed in this report: (1) APF errors and (2) a combined case will all errors. For more detail on other errors, readers are referred to *Himani et. al 2020*.

To show the effect of various errors, we first establish a baseline scenario (Table 1). The baseline configuration is defined as a 1-D 1400-km ground swath over which three nadir-pointed satellites orbit with a constant intersatellite spacing of 2.5 km. The three satellites each take a measurement every 30 km of the swath (defined as the ground sample distance), and these groups of measurements are used to reconstruct a single, enhanced measurement located at the center of their overlapping FoV. Ideally, this should result in roughly 46 reconstructed data points. However, resolution enhancement is not performed within 60 km of the beginning or end of the 1400-km swath in order to keep all radiometer measurements contained within the simulated scene (further outside these bounds and the radiometer FoV would be

outside of the simulated scene). This results in roughly 42 total reconstructed data points over the 1400-km swath. Lines between the reconstructed data points use a simple linear interpolation.

Table 1 — Spacecraft Parameters for Baseline Scenario

Parameter	Value
Inter-Satellite Spacing	2.5 km
Instrument Noise	0 K
Instrument Bias	0 K
Navigation Error	0 m
Attitude Error	0 degrees
APF Error	None
Ground Sampling Distance	30 km

The baseline and remainder of Section 3 will focus on four separate scenes: step, multistep, hotspot, and sine. Fig. 4 shows results for each of these scenes using the baseline case. Linear interpolation is used in between derived estimates to reconstruct a full profile equal to the resolution of truth data. Note that BG has a difficult time with sharp transitions (such as the step), and depending on the sampling distribution around the zero-point ground location, reconstruction is not guaranteed to be symmetric over symmetric features (see hotspot in Fig. 4).
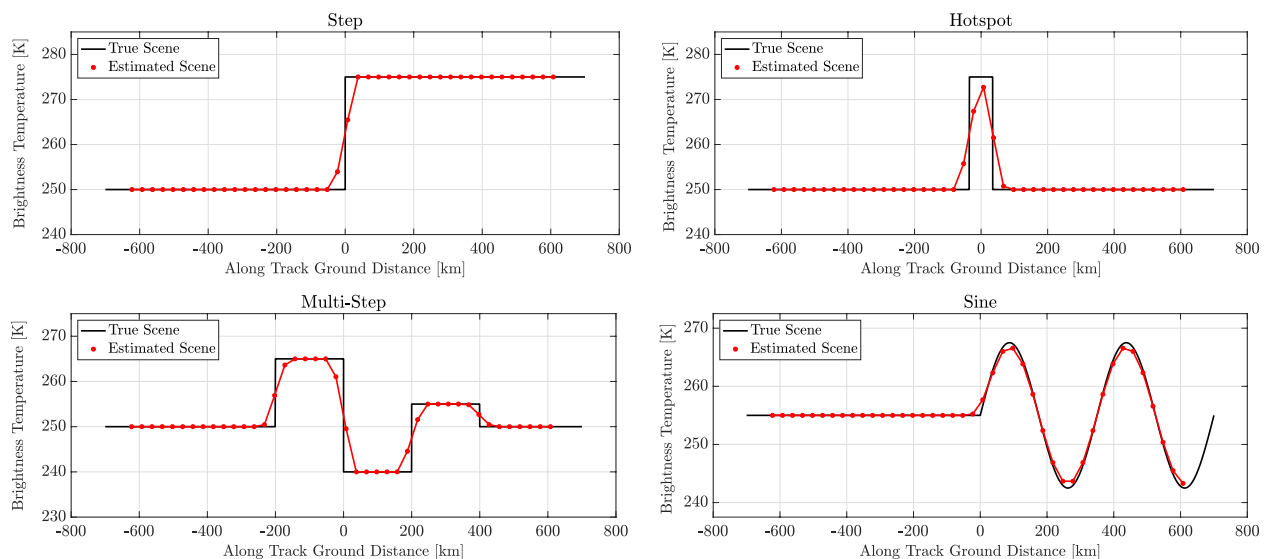

Fig. 4 — Baseline: truth and reconstructed brightness temperature scenes using parameters from Table 1 for (Top Left) step, (Bottom Left) multistep, (Top Right) hotspot, and (Bottom Right) sine.

3.1 Antenna Pattern Function Effects

Next, we consider the effects of imperfect knowledge of an APF in a single spacecraft. While antenna patterns are typically well characterized before launch on flagship-class spacecraft, this characterization could be less stringent for high volume small spacecraft production used in constellations. To implement this mischaracterization, we replace $G(x)$ in (2) with $G_{error}(x)$, where $G_{error}(x)$ is the "true" APF, as shown in Fig. 3. This gives a new set of equations used to derive antenna temperatures for three spacecraft along the entire 1400-km along-track path:

$$T_{A_1} = \int G_{\text{error}}(x)T_B(x)dx + T_{\text{noise}}$$

$$T_{A_2} = \int G(x)T_B(x)dx + T_{\text{noise}}$$

$$T_{A_3} = \int G(x)T_B(x)dx + T_{\text{noise}}$$

Note that only a single spacecraft has the mischaracterization, while the other two do not. Furthermore, the **a** vector calculation still uses the APFs from Fig. 2.

Table 2 shows all error metrics and goodness-of-fit parameters for the baseline case and the APF error case for each scene. In general, reconstruction performance is worse for all metrics and scenes with the exception of standard deviation for the sine scene, where the APF error case slightly outperforms the baseline case.

Table 2 — Error Metrics and Goodness-of-Fit Parameters For All Scenes For Baseline, APF Error, and Combined Error Cases

Scene & Error Type	NSC	Std. Dev [K]	TRA	r^2
Step (Baseline)	0.9801	1.724	179.9	0.9810
Step (APF)	0.9752	1.734	546.5	0.9761
Step (Combined)	0.9681	1.774	746.0	0.9689
Hotspot (Baseline)	0.6988	2.467	361.9	0.8185
Hotspot (APF)	0.6655	2.481	709.0	0.7977
Hotspot (Combined)	0.5939	2.550	914.0	0.7611
Multi (Baseline)	0.8770	2.287	448.6	0.9036
Multi (APF)	0.8625	2.297	730.0	0.8919
Multi (Combined)	0.8429	2.327	886.7	0.8751
Sine (Baseline)	0.9903	1.112	346.3	0.9918
Sine (APF)	0.9857	1.102	559.8	0.9879
Sine (Combined)	0.9711	1.154	721.8	0.9807

3.2   Combined Effects

In order to show how these errors combine to degrade reconstruction performance, we now combine multiple errors. The errors are representative of current small satellite capabilities:
  1) ±0.5 degree random pointing error magnitude on all spacecraft;
  2) 1 K instrument bias on two spacecraft;
  3) 1 K random noise on all TA measurements;
  4) APF mischaracterization on single spacecraft.
Note that, since many of these errors are random, the example shown may not represent a worst case scenario (e.g., all errors cause bias in the same direction). Also, due to the high TRL and flight heritage of GPS receivers, navigation knowledge is assumed to be perfect. Fig. 5 shows the combined error example for all scenes, and Table II shows performance metrics for the reconstructed scenes. As expected, reconstructed scenes in Fig. 5 show both an overall bias and noise on measurements.

The consequences of these combined effects are most prominent in the last step of the multistep scene. The sharp decrease in brightness temperature looks closer to a gradual ramp down around the 400-km mark. As noted earlier, the BG reconstruction has difficulties around sharp transitions but performs well for flat or constantly varying scenes, even in the presence of multiple combined errors.
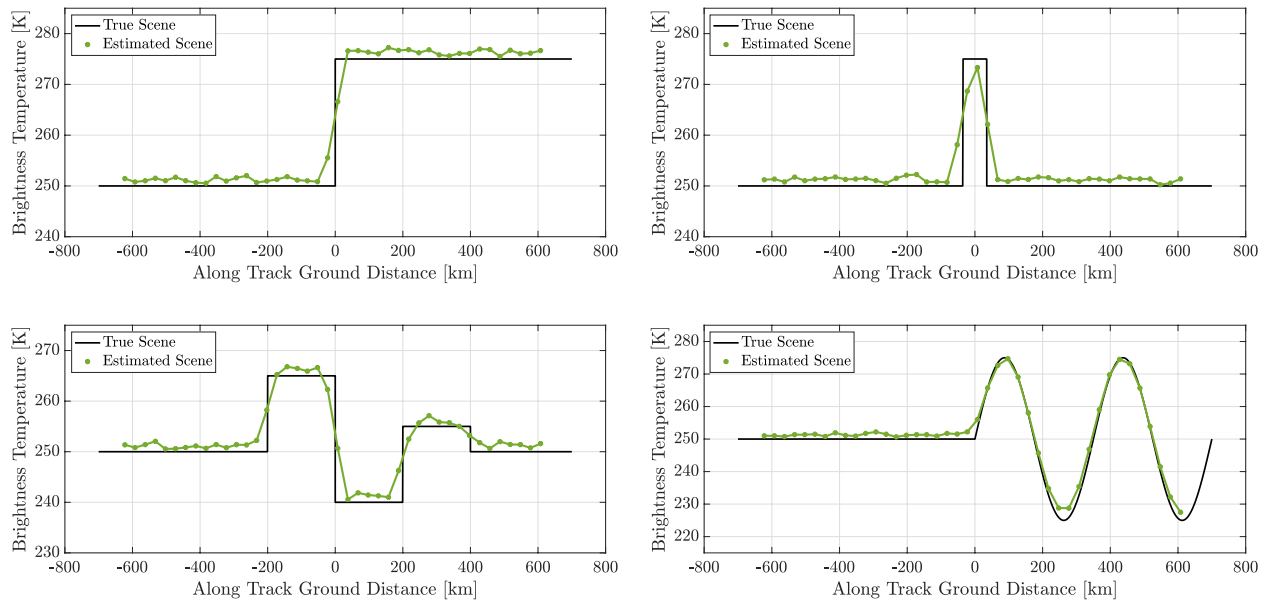
Fig. 5 — Truth and reconstructed brightness temperature scenes using three spacecraft sampling every 30 km with 1 K noise, 1 K bias on two spacecraft, ±0.5° random pointing error, and single spacecraft APF mischaracterization. All other parameters from Table 1 remain constant.

3.3   Subfootprint Scale Features & Time-Varying Brightness Temperatures

With the high sampling density achievable through small spacecraft constellations, we now explore the applicability of the BG method to resolve subfootprint scale features. The resolution, in this case, can be defined as the ability to resolve two closely spaced objects [21]. In the baseline case, the footprint of each sensor APF is 70 km. Fig. 6 shows the original hotspot scene and a dual-hotspot scene (both features now equal in width to the footprint of a single sensor's FoV) estimated using the baseline configuration. From inspection, it is not obvious to detect that subscale features exist in either scene (although a magnitude difference is apparent).
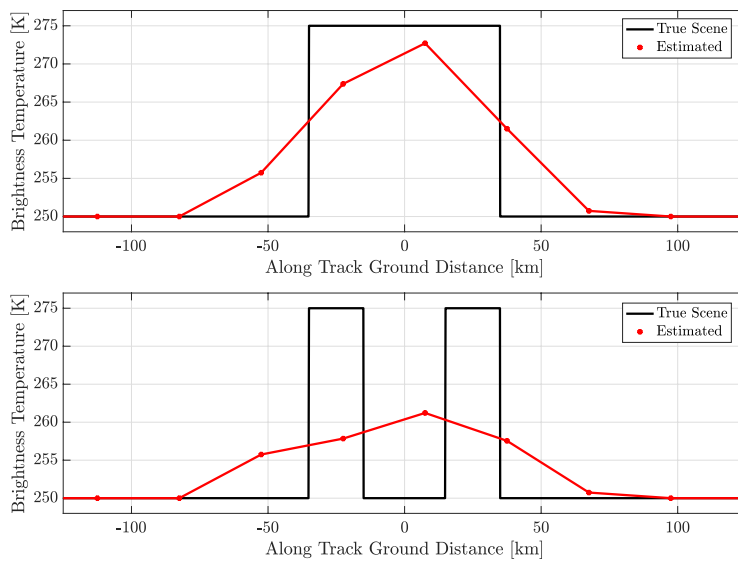

Fig. 6 — (Top) Hotspot and (Bottom) dual-hotspot scenes. All parameters taken from Table 1.

Fig. 7 shows the same scenes estimated using a sample distance of 5 km. The dual-hotspot scene now shows distinct features compared with the hotspot (even if the magnitude of the dual hotspot is lower). While the reconstructed feature does not prove that two hotspots exist in the scene, it does imply that the feature is more diverse than a low magnitude single hotspot. The difference between Figs. 6 and 7 shows the potential of using a high sampling density to extract information about subresolution brightness temperature variations. Operationally, this could lead to improvements in target tasking. For example, small satellite sensors could better identify specific areas to target with high-resolution flagship sensors.
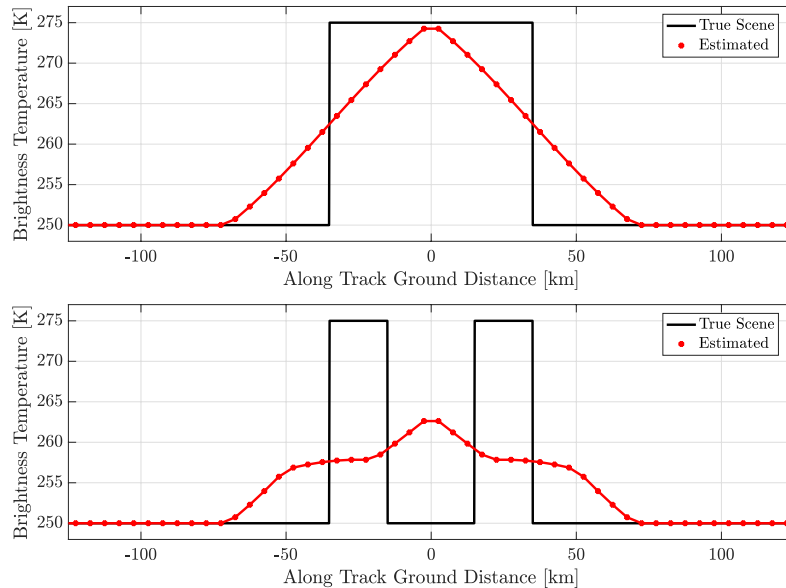

Fig. 7 — (Top) Hotspot and (Bottom) dual-hotspot scenes with 5 km sampling distance. All other parameters taken from Table 1

4.   CONCLUSIONS

A novel distributed geometry was implemented for the well-established BG resolution enhancement reconstruction algorithm. Simulation results show that a distributed architecture is feasible in the 1-D case even in the presence of errors typical of small satellites. These errors affect the reconstruction process in important ways and were quantified through the first known use of NSE for a BG reconstruction. Increasing sampling distance, in general, leads to decreased reconstruction performance. However, this decrease is not monotonic with sampling distance and can be scene-dependent. Adding random antenna temperature noise degrades overall performance. For measurement bias, adding a constant bias to each sensor is the worst case scenario and can be mitigated if sensor bias is random with a constrained magnitude. Although not shown in the above work, navigation and attitude pointing knowledge error tend to shift the reconstructed profiles in the direction of net error magnitude. In both cases, performance degrades monotonically with increasing knowledge error. The mischaracterization of instrument antenna patterns can degrade the performance of reconstruction, with positive and negative errors dependent on the value and magnitude of the integrated gain ratio, R_G. A combined case was presented with multiple errors typical of a small satellite platform. The results for the combined case show that scene portions with low-magnitude sharp transitions (e.g., last step in the multistep scene) are significantly degraded.

Potential avenues for distributed spacecraft architectures were also explored. Because the nature of spacecraft constellations allows for significantly higher sampling densities, subfootprint scale features can be determined to exist, even if they cannot be completely resolved. Time-varying brightness temperature on the order of minutes was shown to damp the performance of reconstruction. Both these avenues could be explored further during potential mission designs.

5. PRELIMINARY WORK FOR 6.1 NEW START

During the second year of the fellowship, Mr. Himani was a Co-I on a 6.1 New Start proposal titled "Fusion of Reflectometry and Radiometry for Satellite Remote Sensing of Surface Soil Moisture" which has since been funded. The goal of the project is to provide a time-series algorithm for surface soil moisture (SSM) retrieval with high temporal resolution and moderate spatial resolution using the Cyclone Global Navigation Satellite System (CYGNSS) constellation. The first year work described in the prior section both aids in the development of this 6.1 and helps extend the prior work using real datasets. The same type of parameters that were modeled and accounted for in the earlier section (attitude, navigation, etc.) will also need to be accounted for when processing CYGNSS data. Specifically, pointing requirements translate into incidence angle corrections that are necessary for physical land parameters (i.e., soil moisture) to be accurately measured. The following sections outline the creation of a data processing pipeline and preliminary results to achieve these types of corrections.

5.1 Data Processing Pipeline

In order to compare the results from the new time-series algorithm derived from the CYGNSS mission, the project needed the capability to process large sets of both CYGNSS data and in-situ validation data. The CYGNSS data is hosted on the NASA Jet Propulsion Laboratory's (JPL) Physical Oceanography Distributed Active Archive Center (PO.DAAC) and the in-situ validation data is hosted by the USDA's Agricultural Research Service (ARS). The ARS data was downloaded locally. Because the CYGNSS dataset is quite large, a processing pipeline was developed such that it can downloaded subsets of the full data set, process the subset to create necessary data products, and delete the raw data. This method saves memory and allows the code to be platform independent.

A MATLAB script was developed to perform this process on CYGNSS Level 1 Normalized Bistatic Radar Cross Section (NBRCS). Since this data product was primarily designed for ocean remote sensing, the NBRCS data needs to be angle-corrected in order to account for the effects of vegetation for surface based soil moisture retrievals [30]. An initial test for the pipeline was to extract NBRCS data over a selected in-situ site (e.g., Walnut Gulch), process it with the angle-correction, plot for a month long time-series. An outline/pseudocode of the processing pipeline is shown below:

1. Pull all data from PO.DAAC server for all 8 satellites for a given day via preferred method
2. Select a satellite and extract all data within specified lat/lon and time bounds. These bounds are obtained based on available data for a specific in-situ site (e.g., Walnut Gulch)
3. Filter necessary data products (lat/lon of specular point, incidence angle, Fresnel coefficients, NBRCS, etc.)
4. Determine time/location of minimum incidence angle
5. Determine Fresnel coefficients and NBRCS at time/location from Step 4
6. Normalize Fresnel coefficient and NBRCS at all times by minimum value derived in Step 5. The process of normalization is outlined in [31]
7. Perform basic data verification process to ensure time and lat/lon of derived quantities are in the bounds outlined in Step 2
8. Export dataset as table and .mat file
9. Repeat 2 through 8 for all satellites in the constellation
10. Delete raw data extracted in Step 1
11. Repeat 1 through 10 for all days of interest

Note that the pseudo-code shown above only applies for the CYNGSS data taken from PO.DAAC and not the in-situ data given by ARS. The process to obtain and process the ARS data is not shown here for brevity.

5.2   Initial Results

Fig. 8 below shows the NBRCS time-series for over the Walnut Gulch site for the first CYGNSS satellite for January 2019 using reflections from the three different GPS satellites.
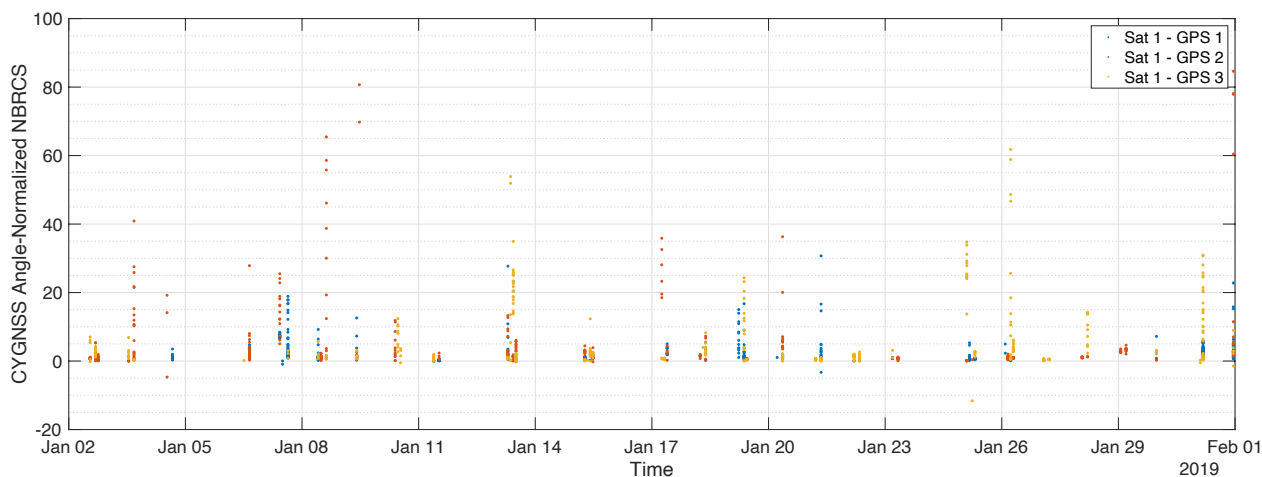

Fig. 8 — CYGNSS satellite 1 incidence angle normalized NBRCS values

Fig. 9 shows the Fresnel coefficients for the first CYGNSS satellite for January 2019 with incidence angle-normalized and non-normalized values. Note that all the values above 0.7 are all normalized. Also, certain normalized NBRCS values are above 1, which typically should not occur. This issue is still being worked on but may be a results of CYGNSS land data collection methods not being as well calibrated compared to ocean retrievals. While no analysis was performed on this data with regard to creating a time-series algorithm, the creation and proof of concept of the processing pipeline is a necessary first step to ensuring the project can start ingesting and processing large sets of CYGNSS data without needing large memory storage systems.
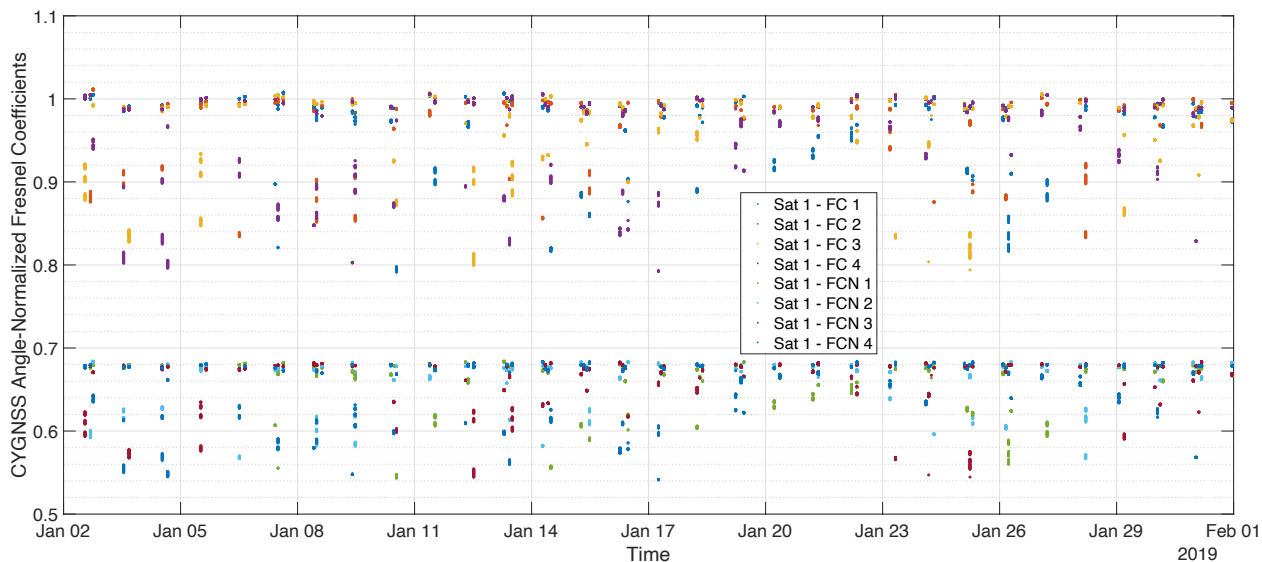

Fig. 9 — CYGNSS satellite 1 incidence angle normalized Fresnel coefficients

6. PUBLICATIONS

Ouellette, J. D., **Himani, T. P.**, Twarog, E. M., & Li, L. (2021). Rough Surface Scattering Model Comparisons for Radar Altimetry of Sea Ice. *IEEE Transactions on Geoscience and Remote Sensing*.

Himani, T., & Jones, A. S. (2020). Microwave Resolution Enhancement Using Distributed Small Spacecraft Architectures. *IEEE Transactions on Geoscience and Remote Sensing*.

Bobak, J., Alqadah, H., Nurnberger, M., Rudolph, S., Bounds, W., & **Himani, T.** (2020). Imaging Algorithm and Measurement Error Impact on Retrievals from the Microwave Single Pixel Imager (MSPI). In *IGARSS 2020-2020 IEEE International Geoscience and Remote Sensing Symposium* (pp. 6551-6554). IEEE

Himani, T. (2020, January). Microwave Resolution Enhancement Using Small Satellite Architectures. In *100th American Meteorological Society Annual Meeting*. AMS

REFERENCES

1. D. Selva and D. Krejci, "A survey and assessment of the capabilities of cubesats for Earth observation," *Acta Astronautica*, vol. 74, pp. 50–68, May 2012.
2. E. Buchen, "Small satellite market observations," in *Proc. Small Satell. Conf.*, 2015, pp. 1–5.
3. Y. Ma, X. Zou, and F. Weng, "Potential applications of small satellite microwave observations for monitoring and predicting global fast- evolving weathers," *IEEE J. Sel. Topics Appl. Earth Observ. Remote Sens.*, vol. 10, no. 6, pp. 2441–2451, Jun. 2017.
4. C. S. Ruf *et al.*, "A new paradigm in Earth environmental monitoring with the CYGNSS small satellite constellation," *Sci. Rep.*, vol. 8, no. 1, p. 8782, Dec. 2018.
5. E. Peral, S. Tanelli, Z. Haddad, O. Sy, G. Stephens, and E. Im, "Raincube: A proposed constellation of precipitation profiling radars in CubeSat," in *Proc. IEEE Int. Geosci. Remote Sens. Symp. (IGARSS)*, Jul. 2015, pp. 1261–1264.
6. S. C. Reising *et al.*, "Overview of temporal experiment for storms and tropical systems (TEMPEST) CubeSat constellation mission," in *IEEE MTT-S Int. Microw. Symp. Dig.*, May 2015, pp. 1–4.
7. W. J. Blackwell *et al.*, "An overview of the TROPICS NASA Earth venture mission," *Quart. J. Roy. Meteorol. Soc.*, vol. 144, no. S1, pp. 16–26, Nov. 2018.
8. S. Nag, C. K. Gatebe, and T. Hilker, "Simulation of multiangular remote sensing products using small satellite formations," *IEEE J. Sel. Topics Appl. Earth Observ. Remote Sens.*, vol. 10, no. 2, pp. 638–653, Feb. 2017.
9. A. Poghosyan and A. Golkar, "CubeSat evolution: Analyzing CubeSat capabilities for conducting science missions," *Prog. Aerosp. Sci.*, vol. 88, pp. 59–83, Jan. 2017.
10. R. Houborg and M. McCabe, "High-resolution NDVI from Planet's constellation of Earth observing nano-satellites: A new data source for precision agriculture," *Remote Sens.*, vol. 8, no. 9, p. 768, Sep. 2016.
11. M. F. McCabe *et al.*, "The future of earth observation in hydrology," *Hydrol. earth Syst. Sci.*, vol. 21, no. 7, p. 3879, 2017.
12. M. Schmitt and X. X. Zhu, "Data fusion and remote sensing: An ever- growing relationship," *IEEE Geosci. Remote Sens. Mag.*, vol. 4, no. 4, pp. 6–23, Dec. 2016.
13. A. Stogryn, "Estimates of brightness temperatures from scanning radiometer data," *IEEE Trans. Antennas Propag.*, vol. AP-26, no. 5, pp. 720–726, Sep. 1978.
14. A. Gambardella and M. Migliaccio, "On the superresolution of microwave scanning radiometer measurements," *IEEE Geosci. Remote Sens. Lett.*, vol. 5, no. 4, pp. 796–800, Oct. 2008.
15. D. G. Long and M. J. Brodzik, "Optimum image formation for space- borne microwave radiometer products," *IEEE Trans. Geosci. Remote Sens.*, vol. 54, no. 5, pp. 2763–2779, May 2016.
16. F. Lenti, F. Nunziata, M. Migliaccio, and G. Rodriguez, "Two- dimensional TSVD to enhance the spatial resolution of radiometer data," *IEEE Trans. Geosci. Remote Sens.*, vol. 52, no. 5, pp. 2450–2458, May 2014.
17. E. Santi, "An application of the SFIM technique to enhance the spatial resolution of spaceborne microwave radiometers," *Int. J. Remote Sens.*, vol. 31, no. 9, pp. 2419–2428, May 2010.
18. M. Alparone, F. Nunziata, C. Estatico, and M. Migliaccio, "A multichan- nel data fusion method to enhance the spatial resolution of microwave radiometer measurements," *IEEE Trans. Geosci. Remote Sens.*, pp. 1–9, 2020.
19. L. Alparone, B. Aiazzi, S. Baronti, and A. Garzelli, *Remote Sensing Image Fusion*. Boca Raton, FL, USA: CRC Press, 2015.
20. J. R. Wertz, D. F. Everett, and J. J. Puschell, *Space Mission Engineering: New SMAD*. Portland, OR, USA: Microcosm Press, 2011.
21. D. G. Long, "Reconstruction and resolution enhancement techniques for microwave sensors," in *Frontiers of Remote Sensing Information Processing*. Singapore: World Scientific, 2003, pp. 255–281.

22. P. J. Stephens and A. S. Jones, "A computationally efficient dis- crete backus-Gilbert footprint-matching algorithm," *IEEE Trans. Geosci. Remote Sens.*, vol. 40, no. 8, pp. 1865–1878, Aug. 2002.
23. G. A. Poe, "Optimum interpolation of imaging microwave radiometer data," *IEEE Trans. Geosci. Remote Sens.*, vol. 28, no. 5, pp. 800–810, 1990.
24. M. R. Farrar and E. A. Smith, "Spatial resolution enhancement of ter- restrial features using deconvolved SSM/I microwave brightness temper- atures," *IEEE Trans. Geosci. Remote Sens.*, vol. 30, no. 2, pp. 349–355, Mar. 1992.
25. J. E. Nash and J. V. Sutcliffe, "River flow forecasting through conceptual models Part I—A discussion of principles," *J. Hydrol.*, vol. 10, no. 3, pp. 282–290, 1970.
26. T. Himani, E. G. Lightsey, C. Coen, M. Frounchi, J. D. Cressler, and W. Williams, "MicroNimbus: A CubeSat mission for millimeter-wave atmospheric temperature profiling," in *Proc. AIAA Aerosp. Sci. Meeting*, Jan. 2018, p. 1941.
27. C. S. Ruf, "Detection of calibration drifts in spaceborne microwave radiometers using a vicarious cold reference," *IEEE Trans. Geosci. Remote Sens.*, vol. 38, no. 1, pp. 44–52, Jan. 2000.
28. S. Q. Kidder and A. S. Jones, "A blended satellite total precipitable water product for operational forecasting," *J. Atmos. Ocean. Technol.*, vol. 24, no. 1, pp. 74–81, Jan. 2007.
29. B. Yost, "State of the art of small spacecraft technology," NASA, Washington, DC, USA, Tech. Rep., Dec. 2018.
30. Al-Khaldi, M. M., Johnson, J. T., O'Brien, A. J., Balenzano, A., & Mattia, F. (2019). Time-series retrieval of soil moisture using CYGNSS. *IEEE Transactions on Geoscience and Remote Sensing*, *57*(7), 4322-4331.